Journal of Science and Technology – Engineering and Technology for Sustainable Development
Volume 36, Issue 1, March 2026, 039-045

Photoresponse Characteristics of Nano-V_2O_5 Material Directly Synthesized from Vanadium Powder via Microwave

Sai Tuan Vu, Nguyen Thanh Nghi, Luong Huu Phuoc, Dang Duc Vuong, Vu Xuan Hien [*]
School of Engineering Physics, Hanoi University of Science and Technology, Ha Noi, Vietnam
[*]*Corresponding author email: hien.vuxuan@hust.edu.vn*

Abstract

Vanadium pentoxide (V_2O_5) was rapidly synthesized from vanadium metal powder using a microwave-assisted method, completing the entire process in less than one hour. The resulting material exhibited a wrinkled nanosheet morphology. The synthesized V_2O_5 showed enhanced photoresponsivity, with the photocurrent increasing by approximately 1.8 times under 470 nm illumination. In addition, the material exhibited excellent ambient stability, with negligible signal degradation after 30 days. Structural and optical properties were systematically characterized by X-ray diffraction (XRD), Raman spectroscopy, and UV–Vis spectroscopy, revealing clear correlations between synthesis conditions, crystal structure, and optical behavior. These findings highlight microwave-assisted synthesis as a fast and efficient strategy for fabricating V_2O_5-based materials for photodetectors and other optoelectronic applications.

Keywords: Nanostructured materials, microwave-assisted synthesis, optical properties, photodetectors, vanadium oxides.

1. Introduction

Vanadium oxides are a versatile family of compounds formed between vanadium and oxygen, noted for their structural diversity and broad range of industrial and scientific applications. Among them, vanadium pentoxide (V_2O_5) is considered the most significant oxide of vanadium. It typically occurs as an orange–yellow solid with an orthorhombic crystal structure. Due to its high oxidation state, V_2O_5 exhibits both amphoteric and oxidizing properties. It is regarded as a promising material for photodetection applications owing to its bandgap energy, which lies within the visible light spectrum (E_g from 2.2 to 2.7 eV) [1], making it a potential candidate for optoelectronic devices. Owing to its strong light–matter interaction, V_2O_5 has emerged as a promising candidate for optical sensors, ranging from light to ultraviolet (UV) detectors to gas sensors based on photocatalytic effects [2].

V_2O_5 nanostructures have been synthesized using a variety of methods, such as chemical vapor deposition [3], magnetron sputtering [4], sol–gel processing [5], electron beam evaporation [6], hydrothermal methods [7], spray pyrolysis [8], and microwave-assisted synthesis [9]. Shuming Yang and colleagues synthesized V_2O_5 nanorods as a platform for optical sensor research, owing to their excellent electrical and optical conductivity properties [2]. Recently, many researchers in the field of photodetection have been actively developing one-dimensional nanostructured V_2O_5 materials. Chen *et al.* designed Metal–Semiconductor–Metal (MSM) photodetector based on V_2O_5 nanostructures using a physical deposition method. They achieved a photoresponse of 0.005 A/W under a 0.1 V bias voltage with 325 nm illumination. Wang *et al.* reported the fabrication of a UV sensor using a high-quality crystalline V_2O_5 thin film deposited on a silicon substrate. Their team observed changes in resistance under an illumination wavelength ratio of 254/365 nm.

These previous studies have demonstrated that, in most earlier works, many researchers primarily employed UV light illumination to fabricate UV photodetectors based on nanostructured V_2O_5, often utilizing high-precision, complex, and energy-intensive techniques. In this study, we propose the synthesis of nanostructured V_2O_5 using a microwave-assisted method, which is simple, rapid, and energy-efficient. Moreover, our research focuses on investigating light illumination within the visible spectrum–a topic that has received limited attention in previous publications.

2. Experimental Details

2.1. V_2O_5 Material Preparation

Synthesis procedure is illustrated in detail in Fig. 1. Initially, 50 mg of vanadium metal powder (V, 99.5% purity, Sanno Co., China) was weighed and transferred into a 100 mL Duran bottle (DWK Life Sciences, Germany). Subsequently, a solution of H_2O_2 (at 30% concentration, Xilong Scientific, China) and deionized water was prepared in a predetermined ratio, with a total volume of 13 mL. This solution was gradually added to the vanadium powder in the bottle. First, 50 mg of

---

p-ISSN 3093-3242
e-ISSN 3093-3579
https://doi.org/10.51316/jst.188.etsd.2026.36.1.6
Received: Jun 23, 2025; Revised: Aug 15, 2025
Accepted: Oct 9, 2025; Online: Feb 5, 2026.

vanadium metal powder was prepared as the starting material. Then, the H_2O_2/H_2O solution was added according to the volume ratios listed in Table 1, forming the reaction mixture. After the solvent was introduced, this mixture was subjected to ultrasonic agitation for 30 mins to ensure uniform dispersion and simultaneously enhance the reaction kinetics. Subsequently, the reaction mixture was placed in a microwave oven and irradiated at a power of 80 W for 5 mins, providing rapid heating and facilitating the completion of the reaction. Finally, the obtained products, corresponding to the H_2O_2/H_2O ratios given in Table 1, were collected as V_2O_5 samples.

Table 1. List of V_2O_5 samples

Sample name	H_2O_2/H_2O (vol./vol.)
V4	4/9
V7	7/6
V9	9/4
V10	10/3
V13	13/0

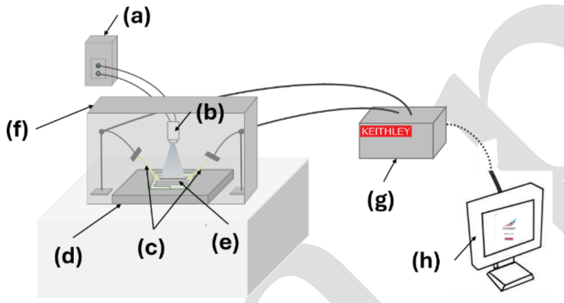

Fig. 1. Schematic of the optical measurement setup: (a) LED power supply, (b) LED source, (c) Probe, (d) Heater, (e) Electrodes, (f) Light-blocking enclosure, (g) Keithley measurement unit, (h) Computer

2.2. Material Characterization

For structural and spectroscopic analyses, the synthesized V_2O_5 solution was drop-cast onto silicon substrates (instead of the photodetector electrodes) and subsequently annealed on a heating stage at 400 °C for 75 minutes. These prepared films were then used for Scanning Electron Microscope (SEM, Hitachi tabletop microscopes TM4000Plus, Hitachi Co., Japan), X-ray Diffraction (XRD; X'Pert-Pro, Malvern Panalytical Ltd, U.K), Raman (Renishaw PLC, U.K), and UV-Vis (UV–vis; Cary 5000 UV–vis–NIR, Agilent, USA) measurements to ensure consistency between the characterized material and the active layers employed in the photodetectors.

2.3. Fabrication of Photodetector Device

The interdigitated electrode used in this study was custom-fabricated at the International Training Institute for Materials Science (ITIMS), Hanoi University of Science and Technology (HUST). The electrode was patterned on a silicon substrate using standard photolithography. Platinum (Pt) was deposited as the electrode material to form an interdigitated structure consisting of 20 fingers. Each finger had a width of 50 µm, a length of 200 µm, and was separated from adjacent fingers by a 50 µm gap.

The sensor device was fabricated by drop-casting the synthesized solution onto an interdigitated electrode. After deposition, the electrode was placed in a drying oven at 80 °C for 15 minutes to allow the solvent to evaporate. Finally, the electrode was annealed on a heating stage at 400 °C for 75 mins to complete the crystallization process and stabilize the coating layer.

The photodetection measurement (Fig. 1) was designed to investigate the change in resistance of vanadium oxide materials under light exposure. The light source used in the setup is an light Emitting Diode (LED) driven at a constant current of 20 mA, providing stable illumination with a wavelength suitable for inducing photoresponse in the oxide layer. The LED is positioned at a fixed distance of 20 mm above the sample, illuminating the sample surface directly. The test samples, consisting of electrodes coated with vanadium oxide, are placed on a heating stage. The entire measurement system–including the electrodes and probe contacts–is enclosed within a sealed metal chamber to eliminate all ambient light interference. This setup ensures that only the LED light interacts with the sample, thereby maximizing measurement accuracy.

3. Results and Discussion

3.1. Structural Characterization of V_2O_5

Fig. 2 shows SEM images of V_2O_5 films synthesized with different H_2O_2/H_2O ratios. All samples exhibit a wrinkled nanosheet-like morphology uniformly covering the substrate, confirming the successful formation of continuous layers. In Fig. 2a (Sample V4, 4/9), the wrinkles appear fine and densely distributed, forming an interconnected network, whereas Fig. 2b (Sample V7, 7/6) shows slightly broader features with occasional branching ridges. The wrinkles in Fig. 2c (Sample V9, 9/4) are relatively uniform in thickness and evenly distributed across the surface, while Fig. 2d (Sample V10, 10/3) presents a more irregular morphology with extended folds and larger uncovered regions, suggesting reduced compactness. Finally, Fig. 2e (Sample V13, 13/0) exhibits the most pronounced wrinkling, with larger protrusions and less homogeneous coverage, likely caused by local stacking during the drop-casting process. Despite these subtle differences, the wrinkle density and characteristic dimensions remain comparable across the samples, indicating that the H_2O_2/H_2O ratio has little effect on the overall surface morphology, with minor variations more likely related to multilayer deposition and drying dynamics.

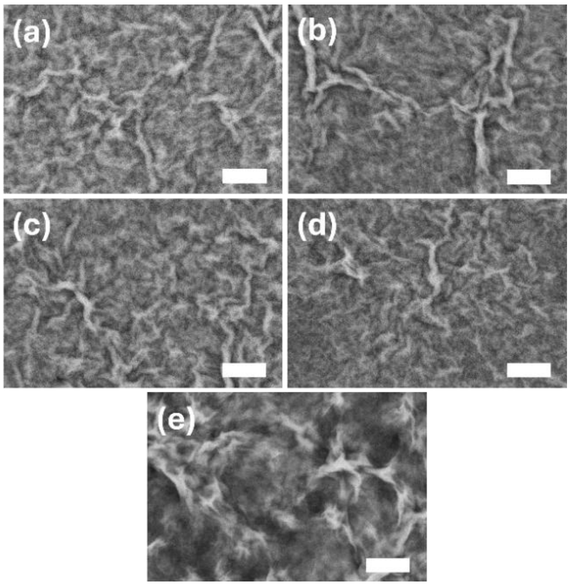

Fig. 2. SEM images of the surface morphology of the samples: (a) Sample V4 (H_2O_2/H_2O = 4/9); (b) Sample V7 (H_2O_2/H_2O = 7/6); (c) Sample V9 (H_2O_2/H_2O = 9/4); (d) Sample V10 (H_2O_2/H_2O = 10/3); (e) Sample V13 (H_2O_2/H_2O = 13/0). The scale bar is 4 µm.

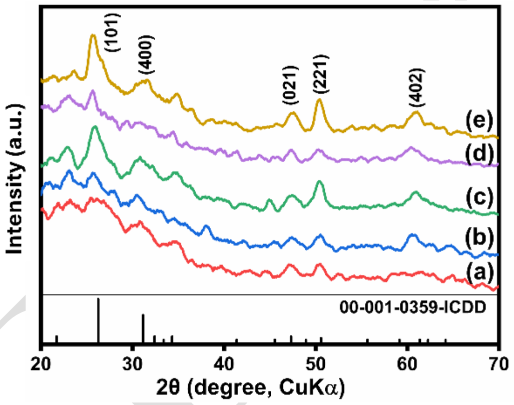

Fig. 3. X-ray diffraction patterns of samples: (a) Sample V4 (H_2O_2/H_2O = 4/9); (b) Sample V7 (H_2O_2/H_2O = 7/6); (c) Sample V9 (H_2O_2/H_2O = 9/4); (d) Sample V10 (H_2O_2/H_2O = 10/3); (e) Sample V13 (H_2O_2/H_2O = 13/0)

The X-ray diffraction (XRD) patterns of the synthesized V_2O_5 samples are shown in Fig. 3. The results indicate that the materials possess an orthorhombic crystal structure, with diffraction peaks observed at 2θ values of 26.5°, 31.2°, 47.5°, 50.4°, and 61.1°, corresponding to the (101), (400), (021), (221), and (402) planes of V_2O_5, respectively, in accordance with the standard ICDD card No. 00-001-0359 [10]. The formation of the V_2O_5 phase in this system is attributed to the oxidation of vanadium metal in H_2O_2 solution, as described by the following reaction [11]:

$$2V + 3H_2O_2 \rightarrow V_2O_5.H_2O + 2H_2O \tag{1}$$

For sample V4 (Fig. 3a), the XRD pattern shows no discernible diffraction peaks across the scanned range, confirming the absence of crystallization and indicating that the material remains essentially amorphous. In contrast, samples V7 (Fig. 3b) and V10 (Fig. 3d) exhibit weak and broad humps centered at approximately 26.5° and 31.2°, which correspond to the main reflections of orthorhombic V_2O_5. The broadness and low intensity of these features suggest incomplete phase formation and a low degree of crystallinity, rather than the development of a well-defined orthorhombic structure. For samples V9 (Fig. 3c) and V13 (Fig. 3e), distinct diffraction peaks assigned to the (101), (221), and (402) planes become more evident, indicating clearer formation of the V_2O_5 phase under synthesis conditions with higher H_2O_2 concentrations. In particular, the (101) reflection at 26.5° appears significantly sharper, confirming enhanced crystallinity relative to the other samples. Nevertheless, the peak intensities remain relatively weak, suggesting either a limited overall crystallinity or the presence of nanoscale crystallite domains. The average crystallite size of sample V9, estimated from the (101) reflection at 2θ equal 26.5° Full Width at Half Maximum (FWHM) = 1.875°, instrumental broadening equal 0.008°) using the Scherrer equation, is approximately 6.9 nm. This result further supports the conclusion that microwave-assisted synthesis under higher H_2O_2 concentrations promotes phase formation but yields only nanocrystalline V_2O_5.

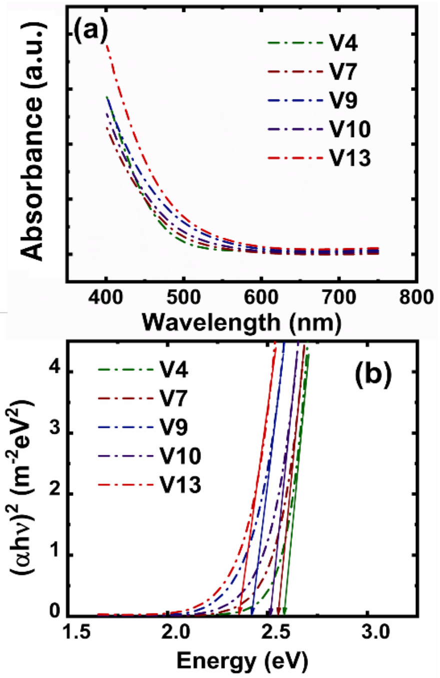

Fig. 4. The absorption curve (a) and Tauc plot (b)

The absorption spectra and optical bandgap widths of the samples, determined using the Tauc method, are presented in Fig. 4. As shown in Fig. 4a, the absorption curves of all samples exhibit a pronounced bend at around 480 nm, corresponding to the photon energy range within the visible region. The optical bandgap energy (E_g) values, shown in Fig. 6b, range from 2.36 eV to 2.57 eV. Specifically, samples V4, V7, and V10 exhibit E_g values of 2.57 eV, 2.55 eV, and 2.51 eV, respectively, while a slight decrease in bandgap energy is observed in samples V9 (2.42 eV) and V13 (2.36 eV), indicating that the synthesis conditions significantly influence the optical properties of the material–particularly through crystallinity, crystal size, and defect density. The narrower bandgap values observed for samples V9 and V13 highlight their strong potential for visible-light photodetection. A reduced bandgap enables absorption of lower-energy photons (i.e., longer wavelengths), thereby extending the spectral response and enhancing the probability of carrier excitation under illumination. This behavior is consistent with the XRD results, where V9 and V13 showed more pronounced reflections of orthorhombic V_2O_5, indicating improved crystallinity compared to the other samples. The nanocrystalline domains, with an estimated crystallite size of approximately 6.9 nm for V9, may further contribute to band structure modifications and effective charge separation. In addition, the wrinkled nanosheet morphology observed in SEM images provides a high surface-to-volume ratio, which facilitates light–matter interaction and improves photon absorption. Taken together, these structural and morphological features explain the reduced bandgap values and support the enhanced photocurrent response observed. Moreover, the measured bandgap values are in good agreement with previously reported ranges for V_2O_5 [12], confirming the reliability of the obtained results and underscoring the applicability of the synthesized materials for visible-light photodetection.

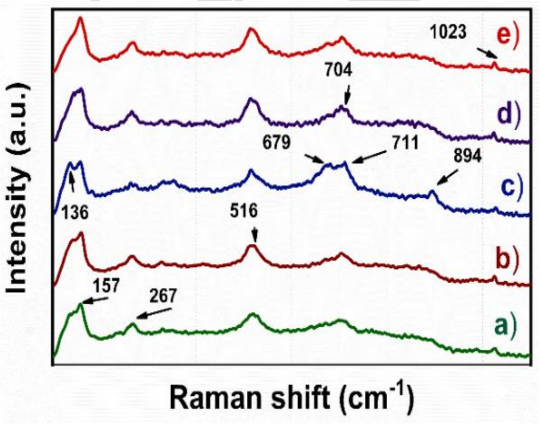

Fig. 5. Raman spectra of the synthesized samples: (a) Sample V4 (H_2O_2/H_2O = 4/9); (b) Sample V7 (H_2O_2/H_2O = 7/6); (c) Sample V9 (H_2O_2/H_2O = 9/4); (d) Sample V10 (H_2O_2/H_2O = 10/3); (e) Sample V13 (H_2O_2/H_2O = 13/0

The Raman spectra of samples from V3 to V13 (Fig. 5) show Raman shift peaks at positions corresponding to different stretching, bending, and other vibrations of V–OH, V–O groups. Most of the samples exhibit vibrations at characteristic wavenumbers, including 157 cm^{-1}, 267 cm^{-1}, 516 cm^{-1}, 704 cm^{-1}, 894 cm^{-1}, and 1023 cm^{-1}. These vibrations represent important bonding features in the vanadium oxide structure.

The intense peak at 157 cm^{-1} corresponds to the stretching vibration between VO_5–VO_5 pyramidal units, indicating a very ordered arrangement of the layers of V–O with relatively distant planes. The 267 cm^{-1} peak is characteristic of the bending vibration of V–O–V. The appearance of the V=O bending vibration begins to indicate a weakening of the V=O bond. At 516 cm^{-1}, the peak corresponds to the stretching vibration of V_3–O, and at 704 cm^{-1}, it corresponds to the stretching vibration of V_2–O. At the highest Raman shift, the peak at 1023 cm^{-1} may correspond to a short V=O bond vibration.

Sample V9 (Fig. 5c) shows a distinct Raman spectrum compared to the other samples. In addition to the usual peaks, it displays a peak at 136 cm^{-1}, often attributed to the lattice vibration and V–O–V bending vibration. An enhancement in the V–OH_2 vibration is shown by an additional peak at 679 cm^{-1}. The high solvation of the sample is reflected in the appearance of a peak at 894 cm^{-1}, corresponding to the V=O stretching vibration.

3.2. Optical Properties

The current–voltage (I–V) characteristics of the V_2O_5 samples, from V4 to V13, are presented in Fig. 8. All samples were evaluated within a voltage range of –5 V to +5 V under three different illumination conditions (470 nm, 530 nm, and 600 nm). In the low-voltage region (approximately –1 V to +1 V), the current increases slowly with applied voltage, indicating that the material exhibits high electrical resistance and behaves as an insulator. However, beyond the threshold of ±3 V, the current rises sharply, clearly demonstrating the nonlinear behavior of the material and reflecting a transition to a conductive state-characteristic of semiconducting behavior.

Upon illumination, all samples exhibited a noticeable change in current. Sample V4 (Fig. 6a) showed a significant increase in current under 470 nm light, indicating effective absorption of short-wavelength light. Sample V7 (Fig. 6b) displayed a distinct behavior compared to the other samples, showing the strongest response under 600 nm illumination. This difference may be attributed to variations in surface structure or the presence of intermediate energy levels. Sample V9 (Fig. 6c) exhibited the highest photocurrent under 470 nm illumination, demonstrating the strongest photoconductive response among all samples, consistent with its SEM-observed surface features. Samples V10 (Fig. 6d) and V13 (Fig. 6e) also responded most strongly to 470 nm light; however, the magnitude of change was smaller than that of V9, which may be explained by incomplete structural formation or enhanced electron–hole recombination processes.

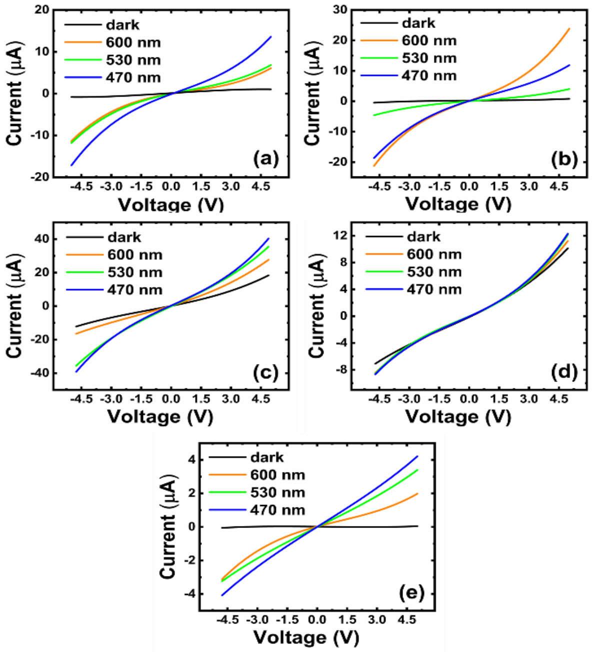

Fig. 6. I–V curves of (a) Sample V4 (H_2O_2/H_2O = 4/9); (b) Sample V7 (H_2O_2/H_2O = 7/6); (c) Sample V9 (H_2O_2/H_2O = 9/4); (d) Sample V10 (H_2O_2/H_2O = 10/3); (e) Sample V13 (H_2O_2/H_2O = 13/0)

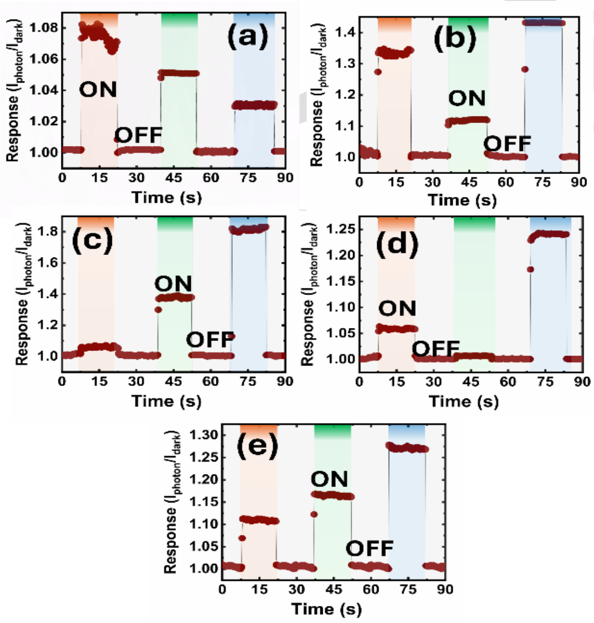

Fig. 7. Photoresponse and wavelength selectivity of (a) Sample V4 (H_2O_2/H_2O = 4/9); (b) Sample V7 (H_2O_2/H_2O = 7/6); (c) Sample V9 (H_2O_2/H_2O = 9/4); (d) Sample V10 (H_2O_2/H_2O = 10/3); (e) Sample V13 (H_2O_2/H_2O = 13/0).

Colored regions indicate light ON periods at specific wavelengths: the left region represents 600 nm, the central region corresponds to 530 nm, and the right region corresponds to 470 nm. White regions indicate light OFF periods.

The photoresponse and wavelength selectivity of the investigated samples are presented in Fig. 7. Sample V4 (Fig. 7a) exhibited negligible variation in photocurrent under different illumination wavelengths. Although a slight increase was observed at 600 nm (approximately 1.08 times higher than in the dark), the overall change was minimal, indicating low photosensitivity and poor wavelength discrimination. Sample V7 (Fig. 7b) showed improved responsivity, with current increases of approximately 1.43 times at 470 nm and 1.35 times at 600 nm, suggesting enhanced light sensitivity. However, the differences between the responses at various wavelengths remained modest, indicating limited wavelength selectivity. Samples V9 and V13 (Fig. 7c and Fig. 7e) demonstrated the strongest response to 470 nm illumination, with sample V9 achieving a responsivity of approximately 1.8 times, indicating efficient light absorption and high photocurrent generation. Sample V13 also exhibited clear photocurrent signals under all three investigated wavelengths, though the intensity was lower than that of V9. Sample V10 (Fig. 7d) showed its highest response at 470 nm (approximately 1.25 times), significantly higher than its response at 600 nm (only about 1.05 times), indicating a more distinct wavelength selectivity compared to the other samples. Overall, most samples displayed better responsiveness to shorter-wavelength light (470 nm) in the visible range; however, their wavelength selectivity remains limited.

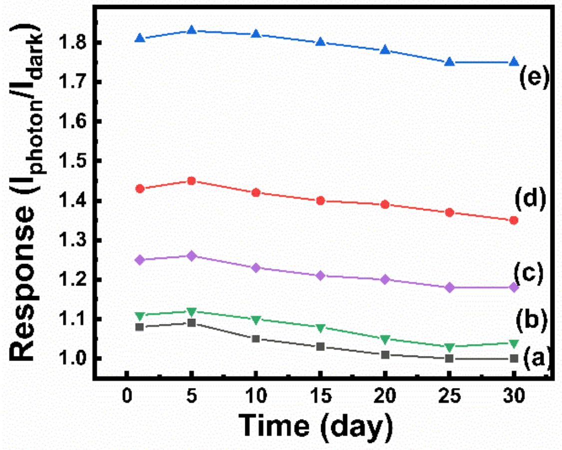

Fig. 8. Stability of (a) Sample V4 (H_2O_2/H_2O = 4/9); (b) Sample V7 (H_2O_2/H_2O = 7/6); (c) Sample V9 (H_2O_2/H_2O = 9/4); (d) Sample V10 (H_2O_2/H_2O = 10/3); (e) Sample V13 (H_2O_2/H_2O = 13/0)

Fig. 8 presents the 30-day photoresponse stability of the V_2O_5 samples under ambient conditions. Measurements were conducted at the wavelength corresponding to the maximum responsivity for each sample: 600 nm for V4 and 470 nm for all others. Samples V4 and V10 exhibited very weak and diminishing photoresponses throughout the testing period. Sample V4 started with a low signal (~1.08) and declined steadily to approximately 1.00 by day 25, showing essentially no detectable photoresponse thereafter. Similarly, V10 decreased from 1.11 to 1.04, indicating a significant loss of photoconductive activity. Although the absolute changes may appear small, these levels are too low to be considered functionally reliable. Thus, these two samples are deemed unsuitable for practical optoelectronic applications.

Samples V7 and V13 maintained moderate photocurrent responses with good consistency over time. V7 declined slightly from 1.43 to 1.35, while V13 dropped from 1.25 to 1.18 across the 30-day period. These gradual reductions suggest that both samples retained a stable photoactive state under ambient conditions, making them viable candidates for applications where moderate responsivity with long-term stability is acceptable. Sample V9 demonstrated the best overall performance, combining high initial responsivity with excellent long-term stability. Its signal decreased only slightly from 1.81 to 1.75 over 30 days. This minor reduction highlights not only the material's efficient photogeneration of carriers but also its structural and chemical durability. Among all samples, V9 is the most promising for practical implementation in optoelectronic devices requiring both sensitivity and stability.

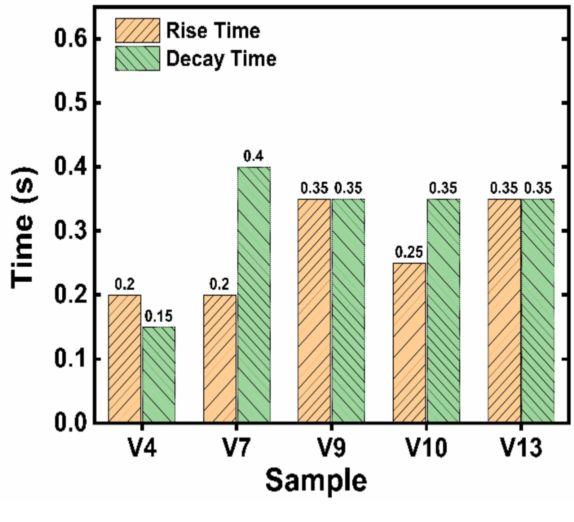

Fig. 9. Comparison of the rise times and the decay times among the samples

As shown in Fig. 9, sample V4 exhibited the shortest response and recovery times, measured at 0.20 s and 0.15 s, respectively. This indicates a rapid response capability, although, as previously noted, this sample possesses low photosensitivity. Sample V7 also demonstrated a short response time (0.20 s), but its recovery time was considerably longer (0.40 s), suggesting an imbalance between the signal activation and recovery processes, potentially related to trap states or intermediate energy levels. For samples V9 (0.35 s – 0.35 s), V10 (0.25 s – 0.35 s), and V13 (0.35 s – 0.35 s), both response and recovery times were elevated and comparatively similar (particularly for V9 and V13), reflecting a slower state transition process despite their relatively high photoresponsivity. Overall, Fig. 9 highlights an inverse correlation between photoresponsivity and response speed, representing a factor that requires careful consideration and optimization.

Theoretically, light with wavelengths shorter than 500 nm should have the ability to excite electrons from the valence band to the conduction band. However, from the observations, it is evident that light with a wavelength of 600 nm, which is longer than 500 nm, can still excite electrons. This is demonstrated by the reduction in the material's resistance when illuminated with 600 nm light. This can be explained through the XRD patterns, where we observe lower peaks and significant noise, indicating that crystallization has not fully occurred, or there are crystal defects that create intermediate energy states. These intermediate states allow electrons to participate in the conduction process, as illustrated in the figure.

SEM images reveal that all samples share a comparable wrinkled-film surface morphology. This similarity indicates that the variations in photonic sensitivity cannot be attributed to major morphological differences across the series. Instead, the enhanced photoresponse observed in selected samples correlates with the more pronounced orthorhombic V_2O_5 reflections in the XRD patterns, suggesting that crystallinity and defect density are the dominant factors governing the optoelectronic behavior. Since the H_2O_2/H_2O ratio affects both crystallization and defect formation, decoupling morphology-specific effects would require a controlled study at fixed composition with varied deposition or annealing conditions, which will be the subject of future investigations.

4. Conclusion

V_2O_5 nanomaterials were rapidly synthesized via a microwave-assisted route in under one hour, yielding wrinkled-film nanostructures with nanoscale features. Structural and spectroscopic analyses (XRD, Raman) confirmed the formation of orthorhombic V_2O_5 with partial crystallinity and characteristic V–O vibrations, while UV–Vis spectra indicated bandgaps of 2.41–2.60 eV, consistent with literature. Photoresponse studies revealed that intermediate H_2O_2/H_2O ratios (notably sample V9) provided the highest sensitivity (approximately 1.8-fold at 470 nm) and excellent stability (a slope of –0.02 over 30 days), whereas extreme ratios resulted in weaker responses. The superior performance of V9 is attributed to its balanced crystallinity and reduced defect density, which favor efficient charge transport under illumination. Overall, these findings demonstrate that controlled synthesis conditions enable tunable optoelectronic properties, making microwave-assisted V_2O_5 nanomaterials promising candidates for visible-light photodetectors.

Acknowledgments

This research is funded by the Ministry of Education and Training under project Code B2024-BKA-04.

References

[1] B. H. Kim, A. Kim, S.-Y. Oh, S. S. Bae, Y. J. Yun, and H. Y. Yu, Energy gap modulation in V_2O_5 nanowires by gas adsorption, Applied Physics Letters, vol. 93, iss. 23, Dec. 2008, Art. no. 233101. https://doi.org/10.1063/1.3044403

[2] S. Shafique, S. Yang, T. Iqbal, B. Cheng, Y. Wang, H. Sarwar, Y. T. Woldu, and P. Ji, Improving the performance of V_2O_5/rGO hybrid nanocomposites for photodetector applications, Sensors Actuators A: Physical, vol. 332, part 1, Dec. 2021, Art. no. 113073. https://doi.org/10.1016/j.sna.2021.113073

[3] J. Musschoot, D. Deduytsche, H. Poelman, J. Haemers, R. L. Van Meirhaeghe, S. Van den Berghe, and C. Detavernier, Comparison of thermal and plasma-enhanced ALD/CVD of vanadium pentoxide, Journal of The Electrochemical Society, vol. 156, no. 7, pp. 122–126, May 2009. https://doi.org/10.1149/1.3133169

[4] C. W. Zou, X. D. Yan, J. Han, R. Q. Chen, and W. Gao, Microstructures and optical properties of β-V_2O_5 nanorods prepared by magnetron sputtering, Journal of Physics D: Applied Physics, vol. 42, no. 14, Jun. 2009, Art. no. 145402. https://doi.org/10.1088/0022-3727/42/14

[5] D. Vasanth Raj, N. Ponpandian, D. Mangalaraj, and C. Viswanathan, Effect of annealing and electrochemical properties of sol-gel dip coated nanocrystalline V_2O_5 thin films, Materials Science in Semicondutor Processing, vol. 16, pp. 256–262, Apr. 2013. https://doi.org/10.1016/j.mssp.2012.09.005

[6] A. Subrahmanyam, Y. B. K. Reddy, and C. L. Nagendra, Nano-vanadium oxide thin films in mixed phase for microbolometer applications, Journal of Physics D: Applied Physics, vol. 41, no. 19, Sep. 2008, Art. no. 195108. https://doi.org/10.1088/0022-3727/41/19/195108

[7] J. Mu, J. Wang, J. Hao, P. Cao, S. Zhao, W. Zeng, B. Miao and S. Xu, Hydrothermal synthesis and electrochemical properties of V_2O_5 nanomaterials with different dimensions, Ceramics International, vol. 41, no. 10, part A, pp. 12626–12632, Dec. 2015. https://doi.org/10.1016/j.ceramint.2015.06.091

[8] L. Kong and I. Taniguchi, Correlation between porous structure and electrochemical properties of porous nanostructured vanadium pentoxide synthesized by novel spray pyrolysis, Journal of Power Sources, vol. 312, pp. 36–44, Apr. 2016. https://doi.org/10.1016/j.jpowsour.2016.02.023

[9] J. Pan, M. Li, Y. Luo, H. Wu, L. Zhong, Q. Wang, and G. Li, Microwave-assisted hydrothermal synthesis of V_2O_5 nanorods assemblies with an improved Li-ion batteries performance, Materials Research Bulletin, vol. 74, pp. 90–95, Feb. 2016. https://doi.org/10.1016/j.materresbull.2015.10.020

[10] S. Kalaiarasi, S. Shyamala, M. Kavitha, and R. R. Muthuchudarkodi, Synthesis and characterization of vanadium oxide nanoparticles with photoluminescent properties, J. Adv. Sci. Res., vol. 13, no. 1, pp. 246–251, 2022. https://doi.org/10.55218/JASR.202213128.

[11] V. X. Hien, V. T. Dong, D. D. Vuong, and N. D. Chien, From microurchins to V_2O_5 nanowalls: improved synthesis through vanadium powder and fast, selective adsorption of methylene blue, Langmuir, vol. 38, iss. 1, pp. 264–274, Dec. 2021. https://doi.org/10.1021/acs.langmuir.1c02461

[12] K. Schneider, Optical properties and electronic structure of V_2O_5, V_2O_3 and VO_2, Journal of Materials Science: Materials in Electronics, vol. 31, pp. 10478–10488, May 2020. https://doi.org/10.1007/s10854-020-03596-0